

See discussions, stats, and author profiles for this publication at: <https://www.researchgate.net/publication/51770731>

Vibrationally Induced Dissociation of Sulfuric Acid (H_2SO_4)

ARTICLE *in* THE JOURNAL OF PHYSICAL CHEMISTRY A · NOVEMBER 2011

Impact Factor: 2.69 · DOI: 10.1021/jp208161y · Source: PubMed

CITATIONS

8

READS

40

2 AUTHORS:



Juvenal Yosa

Universitätsspital Basel

9 PUBLICATIONS 31 CITATIONS

[SEE PROFILE](#)



Markus Meuwly

University of Basel

180 PUBLICATIONS 3,001 CITATIONS

[SEE PROFILE](#)

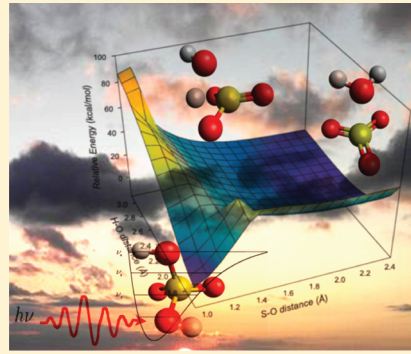
Vibrationally Induced Dissociation of Sulfuric Acid (H_2SO_4)

Juvenal Yosa and Markus Meuwly*

Department of Chemistry, University of Basel, Klingelbergstrasse 80, 4056 Basel, Switzerland

S Supporting Information

ABSTRACT: One of the important reactive steps in Earth's atmosphere is the decomposition of H_2SO_4 to H_2O and SO_3 . However, because the UV spectrum of H_2SO_4 was not found up to 140 nm, alternative mechanisms, including vibrationally induced dissociation, were proposed. Using adiabatic reactive molecular dynamics (ARMD) simulations with validated force fields for the product and educt channels, it is shown through explicit atomistic simulation that by exciting the ν_9 (OH-stretching-) mode, photodissociation can occur on the picosecond time scale. With the potential energy surfaces used in the present work, $\nu_9 = 4$ is sufficient for this process. From a statistically significant number of trajectories (several thousands), vibrationally induced dissociation times are found to follow Gamma-distributions with most likely reaction times between 40 and 200 ps by depositing energies ranging from 40 to 60 kcal/mol, corresponding to 4 and 6 vibrational quanta in the OH stretching vibration. Because ARMD simulations allow multiple and long-time simulations, both nonstatistical, impulsive H-transfer and statistical, IVR-regimes of the decomposition reaction can be discussed in detail at an atomistic level.



I. INTRODUCTION

In the troposphere, sulfur is emitted mainly as sulfur dioxide (SO_2), which is oxidized in the atmosphere to form SO_3 and subsequently hydrolyzed to sulfuric acid (H_2SO_4).^{1,2} This cycling between SO_2 and H_2SO_4 has been studied mainly because it plays an important role in the troposphere aerosol layer formation, which is related to global atmospheric chemistry,³ including cloud condensation⁴ altering the chemical composition and influencing the course of aqueous reactions in clouds. Recent experiments have shown that formation rates and H_2SO_4 concentrations are comparable to those found in the atmosphere, supporting the idea that sulfuric acid is involved in the nucleation of atmospheric aerosols.⁵ The mechanisms and pathways involved in the dissociation of H_2SO_4 to SO_3 and H_2O are still debated. Initially, it was assumed that hydrolysis occurs via absorption of ultraviolet (UV) radiation to produce a dissociative electronically excited state.⁶ However, the electronic absorption spectrum of H_2SO_4 up to 140 nm could not be found experimentally.⁷ In addition, UV photons are absorbed at higher altitudes.⁸ Consequently, only few photons penetrate into the atmosphere with wavelengths shorter than 179 nm,⁹ and UV photodissociation of H_2SO_4 is unlikely to occur at lower altitudes.¹⁰

Following this, it was proposed that some OH-containing species in the atmosphere, including HONO , HONO_2 , or HO_2NO_2 , absorb visible radiation and induce vibrational overtone transitions to states with several quanta in the OH stretching vibration.¹¹ Related calculations suggest that dissociation of H_2SO_4 is possible mainly from highly excited OH-stretching vibrational overtones,¹⁰ which has been also proposed to occur for HNO_x systems.¹² Experimentally, the asymmetric OH stretching vibration ν_9 with $\nu_9 = 4$ and $\nu_9 = 5$ has been characterized by using cavity ring-down spectroscopy, but vibrational photodissociation

of H_2SO_4 has as yet not been observed directly.¹³ The vibrational overtones were found at 13490 and 16494 cm^{-1} , which correspond to 38.57 and 47.16 kcal/mol, respectively. The barrier for sulfuric acid hydrolysis is predicted to be between 32 and 40 kcal/mol ($\approx 12600 \text{ cm}^{-1}$), which opens the possibility for vibrationally induced photodissociation.^{2,14}

Because experimentally the vibrationally induced decomposition reaction $\text{H}_2\text{SO}_4 \rightarrow \text{SO}_3 + \text{H}_2\text{O}$ was not directly observed, computational studies were used to address this problem. A pioneering atomistic simulation at the PM3 level investigated the dynamics of vibrationally excited sulfuric acid by depositing 21 511 cm^{-1} (61.5 kcal/mol corresponding to $\nu_9 = 6$ quanta^{15,16}) of vibrational energy, and the subsequent dynamics was followed for ~ 100 trajectories.¹⁵ In 5% of the cases, photodissociation was found to take place with an average reaction time of 9 ps. However, the number of trajectories that could be run and analyzed was too small to arrive at a conclusive picture due to the high computational effort involved in MD/PM3 simulations.¹⁵ Subsequently, Rice–Ramsperger–Kassel–Marcus theory (RRKM) was used to calculate rate constants (k_{RRKM}) assuming a statistical energy distribution in the excited state.¹⁷ Together with an estimate of the vibrational de-excitation rate, $k_{\text{collision}}$, the behavior of H_2SO_4 after excitation at different altitudes was studied. This work showed that the photodissociation quantum yield increases with altitude and that, at high altitude (above 35 km), the low pressure slows down collisional vibrational relaxation.

In order to treat both possible limits—statistical (RRKM-like) and nonstatistical (impulsive) reactions¹⁸—on an equal footing,

Received: August 24, 2011

Revised: November 2, 2011

Published: November 04, 2011

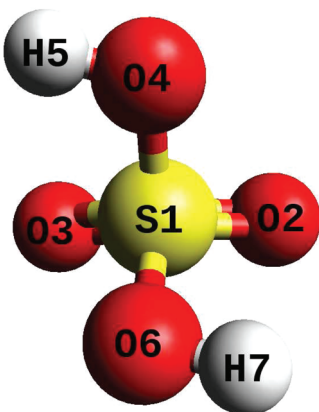


Figure 1. Minimum energy structure (C_2 symmetry) for H_2SO_4 together with atom labeling.

the current work uses adiabatic reactive molecular dynamics (ARMD)^{19–22} to investigate vibrationally induced H_2SO_4 decomposition from a statistically significant number of molecular dynamics (MD) trajectories. ARMD is a surface-crossing algorithm that allows one to follow bond-breaking and bond-forming processes in MD simulations. Because the method was developed for empirical force fields, extensive sampling of phase space is possible. To complement the study, simulations based on the semiempirical self-consistent charges-density functional tight binding (SCC-DFTB) level are also carried out and analyzed.

II. THEORETICAL AND EXPERIMENTAL METHODS

A. MD Simulations. All MD simulations were carried out with CHARMM²³ with provisions for bond-breaking and bond-formation through ARMD.¹⁹ In addition, several hundred “on the fly” MD simulations with SCC-DFTB (see below) were run for up to 1 ns. Starting from a geometry optimized structure of H_2SO_4 (see Figure 1) with 1000 steps of steepest descent minimization, the system was heated to 300 K. The equations of motion were propagated with a leapfrog Verlet algorithm with a time step of $\Delta t = 0.1$ fs during 40 ps and equilibrated for 40 ps, followed by 50 ps of free dynamics simulations in the NVE ensemble. Vibrational excitation was induced by preparing a nonequilibrium state, which corresponds to depositing a specific amount of energy into the relevant degrees of freedom. Different schemes to prepare nonequilibrium initial conditions exist.²⁴ One attractive possibility is to scale the instantaneous velocity vector along the normal mode direction corresponding to the mode of interest. Alternatively, both positions and velocities can be scaled. The first approach—previously and successfully used to, e.g., study proton transfer in small H-bonded complexes²⁵—assumes that the entire excitation is converted into kinetic energy, whereas the second method uses modifications in both the kinetic and potential energies to prepare a nonequilibrium state. One possible drawback of modifying both positions and momenta is the fact that, after excitation, a short equilibration period (a few picoseconds) is required to avoid artifacts due to close proximity of atoms.²⁴ On the other hand, such an approach is probably more general. In the present work, the nonequilibrium state was prepared according to the first scheme, i.e., scaling the instantaneous velocity vector along the normal mode v_9 with energies of 13490 and 16494 cm^{-1} (38.57 and 47.16 kcal/mol) from experiment¹³ and 21511 cm^{-1} (61.5 kcal/mol) estimated from

computation.¹⁵ After this nonequilibrium preparation, 5000 independent ARMD trajectories in the NVE ensemble were run for 0.1–1 ns depending on the level of excitation.

For the simulations in a water droplet, H_2SO_4 was solvated within a sphere of radius 16 Å of TIP3P water.²⁶ Spherical boundary conditions were applied to avoid dissociation of the droplet. The restraining potential is a quartic polynomial $k\delta^2(\delta^2 - V_p)$ where $\delta = r - r_{\text{off}}$, $k = 0.2$ kcal/(mol Å⁴), r is the distance of the restraint atom from the center of the simulation sphere, and V_p is an offset value taken to be 2.25 Å². The cutoff distance $r_{\text{off}} = 16$ Å corresponds to the size of the droplet. Again, the O6–H7 bond is vibrationally excited in the same fashion as for the gas phase simulations. In order to maintain the H_2SO_4 molecule near the center of the sphere, a weak harmonic constraint was applied with a force constant of 0.5 kcal/mol/Å². Upon vibrational excitation the boundary of the water sphere was set to $r_{\text{off}} = 25$ Å to allow expansion of the water droplet.

B. Force Fields for Educt and Product States. In order to study vibrationally induced dissociation of H_2SO_4 , a suitably parametrized force field is required. For this, electronic structure calculations were carried out with Gaussian 03 at the MP2/6-311G++(2d,2p) level of theory in the gas phase.²⁷ Initially, the structures of H_2SO_4 and the product $\text{SO}_3 + \text{H}_2\text{O}$ were optimized. Equilibrium parameters and force constants for bonds and angles were obtained from optimized structures and five single point electronic structure calculations along each of the internal coordinates. Gradients required for the force constants were evaluated from the five-point rule. Mulliken charges were determined on the MP2-optimized structure (see Figure 1 and Table S-I, Supporting Information). To allow bond breaking (distances O4–S1 and O6–H7 in H_2SO_4) and bond formation (O4–H7 for water), Morse potentials were employed:

$$V(r) = D_e(1 - e^{-\beta(r - r_e)})^2 \quad (1)$$

Here, r is the distance between the atoms involved in the bond, D_e is the dissociation energy, β controls the steepness and width of the potential, and r_e is the equilibrium distance. The parameters D_e , β , and r_e were obtained by fitting Morse potentials to the energies which yields the parameters given in Table S-II (Supporting Information). Equilibrium distances and dissociation energies were obtained from relaxed energy scans along the respective coordinate r from 20 steps between 1.0 and 3.0 Å for O4–S1 and 16 steps between 0.5 and 2.0 Å for the O6–H7 distance. All remaining bonds are represented by harmonic potentials. The parametrization for the water molecule in the product state ($\text{SO}_3 + \text{H}_2\text{O}$) followed similar procedures, and the parameters are given in Table S-III (Supporting Information). However, it should be noted that the simulations are not sensitive to the particular parametrization in the product channel, as dissociation is irreversible.

Force field parameters for dihedral angles O2–S1–O4–H5 and H5–O4–S1–O6 were obtained by fitting to energies from relaxed scans starting from the stable C_s conformer and using increments of 10° each. Subsequently, the standard CHARMM force field terms for dihedral angles were fitted using I-NoLLS²⁸ and the CHARMM/I-NoLLS front end.²⁹ For van der Waals interactions, Lennard-Jones potentials with standard CHARMM parameters were initially used. However, as will be discussed further below, ARMD simulations require revised van der Waals parameters for atoms involved in the reaction.

With a validated force field, the only free parameter in ARMD is Δ , which describes the energy difference between the product

Table 1. Optimized Geometry of Educt (H_2SO_4) and Product $\text{SO}_3 + \text{H}_2\text{O}$ Calculated with SCC-DFTB, MP2(full)/6-31G(d,p), and Force Field

bonds [Å]	Educt (H_2SO_4)		
	MP2	CHARMM	SCC-DFTB
H7—O6	0.97	0.97	0.97
O6—S1	1.60	1.60	1.65
H5—O4	0.97	0.97	0.97
S1—O4	1.60	1.60	1.65
S1—O2	1.43	1.43	1.45
S1—O3	1.43	1.43	1.45
angles [°]			
S1—O4—H5	107.5	110.1	116.3
S1—O6—H7	107.5	110.1	116.3
O3—S1—O2	124.7	124.4	123.3
O3—S1—O4	108.7	106.1	109.8
O2—S1—O4	105.2	108.0	105.1
O6—S1—O4	101.7	101.5	101.8
O6—S1—O3	105.3	108.0	105.1
O6—S1—O2	108.7	106.1	109.8
Product ($\text{SO}_3 + \text{H}_2\text{O}$)			
bond [Å]	MP2	CHARMM	SCC-DFTB
S1—O3	1.43	1.43	1.46
S1—O2	1.43	1.43	1.46
S1—O4	1.43	1.43	1.45
O6—H7	0.96	0.96	0.97
O6—H5	0.96	0.96	0.97
angle [°]			
O3—S1—O2	119.9	119.3	119.5
O2—S1—O4	119.9	119.3	120.0
O4—S1—O3	119.9	119.3	120.0
H7—O6—H5	104.1	104.1	108.0

and the educt channels.¹⁹ This energy difference encompasses two contributions: (i) the asymptotic energy difference between the states involved and (ii) a contribution from the fact that the zero of energies for the force fields for the states involved do not coincide. MP2 calculations show that the asymptotic energy difference is 18.7 kcal/mol, which yields $\Delta = 95.0$ kcal/mol. With this value, the asymptotic energy difference between the force fields for H_2SO_4 and SO_3 and H_2O is 18.0 kcal/mol, which is sufficiently accurate for the following.

To compare the structure, activation energy, and reaction path, the transition state (TS) structure was calculated using quadratic synchronous transit-guided (QST2) calculations,³⁰ and the reaction path was followed from intrinsic reaction coordinate (IRC) calculations.³¹ Complementary to the ab initio calculations, potential energy profiles and optimized structures were also determined from semiempirical SCC-DFTB calculations.³² Such an approach also allows one to carry out SCC-DFTB/MD simulations and to compare reaction probabilities with those obtained from ARMD.

III. RESULTS

A. Validation of the Force Field. The energy-minimized structure using the force field leads to a C_2 -symmetric structure

(see Figure 1).³³ A comparison of important bond lengths, angles and dihedral angles between educt and product structures, optimized from MP2, SCC-DFTB, and force field calculations, is summarized in Table 1. The root-mean-square deviation (rmsd) between the force field or SCC-DFTB and MP2 are 0.08 and 0.69 Å for educt and 0.13 and 0.50 Å for products, respectively. This suggests that the force field is parametrized in a meaningful way, and it reproduces MP2 geometries better than SCC-DFTB on average. For bonds, the difference between force field and MP2 calculations is 0.03 Å, whereas for angles it is 3° (see Table 1).

In the dynamics simulations discussed further below, it was found that the parametrization of the dihedral angles O2—S1—O4—H5 and H5—O4—S1—O6 requires particular attention. Previous computational work on rotamers for sulfuric acid revealed the existence of two minimum energy geometries (C_2 and C_s) and two saddle points separating them.^{34,35} In order to capture these effects, a more detailed parametrization strategy was pursued (see Theoretical and Experimental Methods). Figure 2 compares potential energy profiles for relaxed scans along the two dihedral angles for the force field, MP2, and SCC-DFTB calculations. The force field calculations find the higher saddle point 4 kcal/mol above the most stable structure (C_2 symmetry), whereas the second saddle point is 1.8 kcal/mol less stable. This is in good agreement with previous studies^{34,35} and with the present MP2 calculations. It is also found that the force field is able to better capture the potential energy surface (PES) for the H_2SO_4 rotamers than SCC-DFTB (Figure 2).

Additional validations of the force field for H_2SO_4 were carried out for the OH-stretch overtones. Treating the OH-mode as a localized mode with the OH-reduced mass, the Morse potential yields frequencies of 3701 cm^{-1} for the ν_9 fundamental and $14583, 17427, 20103$, and 22683 cm^{-1} for 4, 5, 6, and 7 quanta, respectively. The fundamental overestimates the experimental value of 3609 cm^{-1} by $\sim 100\text{ cm}^{-1}$, and differences for overtones are correspondingly larger. Additional information can be gained from explicit MD simulations. To this end, 30 independent simulations, each 250 ps in length, were carried out at 300 K. The center of the power spectra of the OH-mode for the fundamental and overtones with 4, 5, 6, and 7 quanta peak at $3703, 14713, 17367, 20075$, and 22706 cm^{-1} . These values are similar to those calculated from the Morse potential, which indicates that the OH-mode is indeed quite localized. Additional improvements to the force field are certainly possible to make the parametrization spectroscopically accurate, which, however, was not the purpose of the present work. It should be noted that previous work found an excitation energy of 19289.5 cm^{-1} (55.15 kcal/mol) for $\nu_9 = 6$ at the CCSD(T) level,³⁶ which compares with 57.39 kcal/mol from the present work. As we are primarily concerned with the vibrationally induced dynamics following the deposition of a specific amount of energy, and to avoid confusion, we will refer to “excitation of $\nu_9 = 6$ ” upon delivering 61.5 kcal/mol (original PM3 energy for $\nu_9 = 6$) of energy. However, it should be noted that for the force field used in the present work, 61.5 kcal/mol corresponds to an excitation level closer to $\nu_9 = 7$.

As a final experimental observable the H_2SO_4 dipole moment was calculated from the force field and from SCC-DFTB for an ensemble of 10000 snapshots from an equilibrium simulation. The values are $\mu = 2.69 \pm 0.54$ D and 3.71 ± 0.56 D, compared with 3.41 D from MP2/6-31G++(2d,2p) calculations and 2.30 D from experiment.³⁷ Thus, the force field parametrization best reproduces the dipole moment. However, again, the dipole moment is only of limited relevance for the present work which

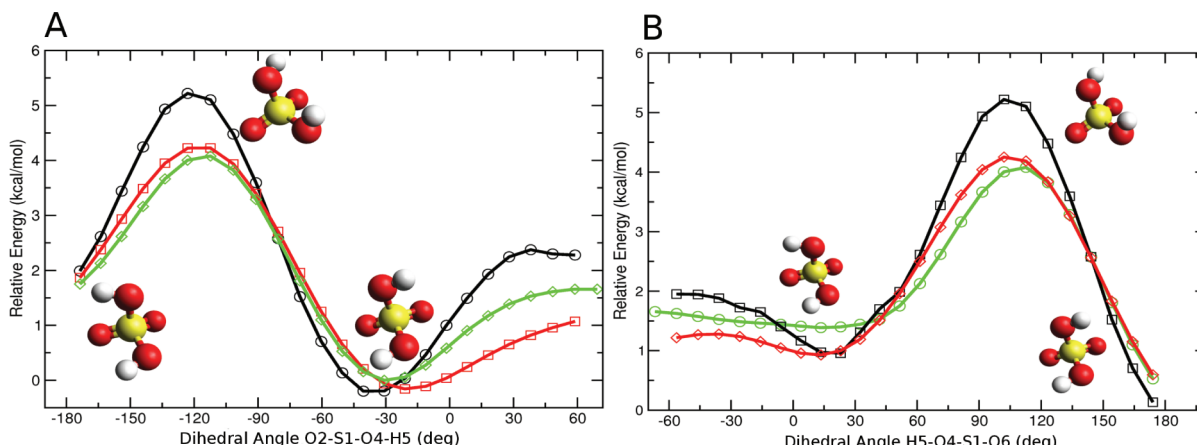


Figure 2. PES along dihedral angles H5–O4–S1–O6 (A) and O2–S1–O4–H5 (B) from MP2 (green), the force field (red), and SCC-DFTB (black).

is concerned with the investigation of vibrationally induced photodissociation.

B. Parametrization of van der Waals Interactions. In conventional force fields, van der Waals interactions are represented by Lennard-Jones potentials

$$V(r) = \varepsilon[(\sigma/r)^{12} - 2(\sigma/r)^6] \quad (2)$$

Here, the r^{12} term represents short-range repulsion due to overlap of electron orbitals, and the r^6 term describes dispersion interactions at long-range. In ARMD, the covalent bond between two atoms is replaced by nonbonded interactions upon breaking, which is determined from an energy criterion involving the entire system.¹⁹ Because the instantaneous “bound” configuration can be quite different from a typical “dissociated” configuration, this can lead to large energy changes upon dissociation. If the standard van der Waals parameters are used upon breaking the chemical bond, the two atoms are likely to partially overlap. For atom separations deep within the bonded region, the notion of nonbonded interactions (as done in force fields) is not meaningful. Thus, for dissociating bonds in ARMD the van der Waals parameters need to be adapted to avoid artificial speedup of the separating atoms/moieties.

To determine meaningful van der Waals- σ values for atoms involved in forming and breaking bonds (the O6–H7 and S1–O4 bonds), ARMD simulation were carried out. Figure S1 (Supporting Information) shows the O6–H7 (A) and S1–O4 (B) separation as a function of time after dissociation for different van der Waals ranges. Rapid increase of internuclear distances between atoms indicates a strong and instantaneous repulsion upon switching the force fields—based on ARMD¹⁹—from the bound (H_2SO_4) to the dissociated ($\text{SO}_3 + \text{H}_2\text{O}$) state. This rapid increase is, however, an artifact of using separately parametrized force fields for the bound and dissociated states, respectively. To avoid such artifacts, the van der Waals ranges σ of the atoms involved in the O6–H7 and S1–O4 interaction are gradually reduced. This leads to the following changes in the van der Waals ranges (see Table S-IV (Supporting Information)) for which no artifact in the dynamics upon breaking the bond was observed: from $R_{\min}^{\text{H}}/2 = 0.23 \text{ \AA}$, $R_{\min}^{\text{O}}/2 = 1.77 \text{ \AA}$, and $R_{\min}^{\text{S}}/2 = 2.00 \text{ \AA}$ for the H, O, and S atoms to $R_{\min,\text{new}}^{\text{H}}/2 = 0.22 \text{ \AA}$, $R_{\min,\text{new}}^{\text{O}}/2 = 1.22 \text{ \AA}$, and $R_{\min,\text{new}}^{\text{S}}/2 = 1.30 \text{ \AA}$. This corresponds to a reduction of the σ values for the O–S and O–H pairs by 44 and 26%, respectively. Interestingly these σ values ($\sigma(\text{S}–\text{O}) = 2.52$ and $\sigma(\text{O}–\text{H}) = 1.44$)

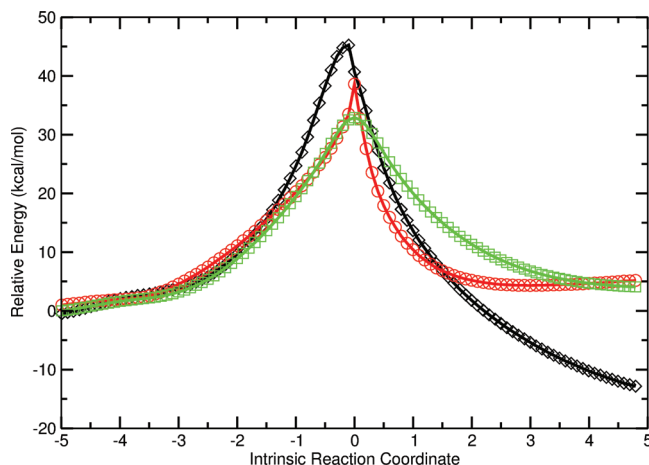


Figure 3. Reaction path for H_2SO_4 hydrolysis. Structure numbers correspond to those structures that follow the reaction path in IRC calculation at the MP2 level. Here each structure from MP2 was taken, and single point energy was evaluated using force field and SCC-DFTB. Black represents calculations using SCC-DFTB, red is for force field, and green is for MP2. The barriers from MP2, force field, and SCC-DFTB are 32.8, 40.0, and 45 kcal/mol, respectively.

are close to the O–S distance in $\text{H}_2\text{O}–\text{SO}_3$ of 2.42 Å in the product state and O–H distance (1.23 Å) in the TS, which supports the empirical adjustment of the van der Waals radii described above.

C. Geometry of the TS. Ab initio calculations for the TS between H_2SO_4 and $\text{SO}_3+\text{H}_2\text{O}$ yielded structures comparable to those reported earlier.^{2,14} Here, the barrier is 32.9 kcal/mol (including zero point energy corrections) compared to 32.2 kcal/mol from previous calculations.¹⁴ Figure 3 reports the energy barrier from IRC calculations in the gas phase together with structures of the product, educt, and TS geometries.

Structures along the reaction path were used to evaluate the force field energy and that from SCC-DFTB. This allows one to compare the activation energy and to further validate the force field (see Figure 3). It is found that the overall shape of the PES connecting educt and product through the TS from the force field is in quite good agreement with the MP2 calculations. The relative energies of products and educts agree to within 2 kcal/mol, whereas the forward barrier is overestimated by 7.2 kcal/mol.

Table 2. Comparison for TS Structure for H_2SO_4 from the Different Methods

coordinate	literature ¹⁴	MP2	force field ^a	SCC-DFTB
bonds [Å]				
O4—H5	0.97	0.97	1.02 ± 0.03	1.05
S1—O4	1.92	1.89	1.87 ± 0.01	2.01
O4—H7	1.24	1.25	1.33 ± 0.04	1.09
O6—H7	1.24	1.25	1.18 ± 0.03	1.28
S1—O6	1.53	1.52	1.49 ± 0.02	1.59
angle [deg]				
S1—O4—H5	110.8	106.6	110.9 ± 7.6	105.0
S1—O4—H5	66.9	67.7	64.4 ± 8.2	63.2
O4—S1—O6	80.4	81.6	87.2 ± 6.2	74.9

^a For the force field calculations averages over 50 snapshots are reported.

Thus, all rates reported in the following are likely to be too slow. Toward the product channel the profiles start to deviate from each other. However, this is of less concern, as we are primarily interested in the decomposition reaction. SCC-DFTB also follows the MP2 energy profile quite closely but leads to a higher TS energy (by 12.2 kcal/mol) than MP2. On the product side, SCC-DFTB has a very different PES profile compared to MP2. However, this again does not affect the conclusions for the dissociation reaction. The structure of the TS obtained by ARMD is also near those obtained by MP2 calculations and reported previously (see Table 2).¹⁴

The PES for hydrolysis of H_2SO_4 as a function of the O6—H7 and S1—O4 distances at the MP2/6-311G++(2d,2p) level is shown in Figure 4. It is of interest to consider projections of reactive trajectories onto this surface in order to better understand how the reactive seam is crossed. As will be described later, excitation of $\nu_9 = 5$ leads to a broad distribution of reaction times ranging from a few to hundreds of picoseconds. From all the reactive trajectories calculated with ARMD, 10 with short, intermediate, and long reaction times were randomly chosen. They correspond to reaction times of $\tau \approx 5$, 250, and 600 ps and are also shown in Figure 4. Trajectories with $\tau \approx 5$ ps (white) show pronounced stretching movement along the vibrationally excited (O6—H7) bond and rapidly cross the energy barrier without transferring appreciable amounts of energy into the S1—O4 bond. Due to the high vibrational excitation energy, rapid dissociation occurs, and the trajectory does not cross the reactive seam at the TS but away from it. The system explores energy regions uphill before dissociating into $\text{SO}_3 + \text{H}_2\text{O}$. Trajectories with $\tau \approx 250$ and 600 ps (green and red), show energy transfer into the (S1—O4) stretching mode but to different extents. The crossing of the reactive seam is also very rapid, but the distribution of crossing geometries is much wider compared to trajectories with early reaction times.

D. Reaction Dynamics. With a validated force field (correct product/educt geometries, qualitatively correct shape, and TS energy of PES), atomistic simulations can now be run to collect a statistically significant number of independent trajectories and to analyze the geometrical, energetic, and temporal aspects of vibrationally induced dissociation in H_2SO_4 . In order to follow the temporal evolution of the system following vibrational excitation, ARMD simulations were carried out (see Theoretical and Experimental Methods). The parametrization presented so far allows two product states to be populated: dissociation into $\text{SO}_3 + \text{H}_2\text{O}$ and $\text{SO}_3 + \text{OH} + \text{H}$. However, the dissociation energy of water into $\text{OH} + \text{H}$ in the gas phase is 117 kcal/mol,^{38,39} which has to

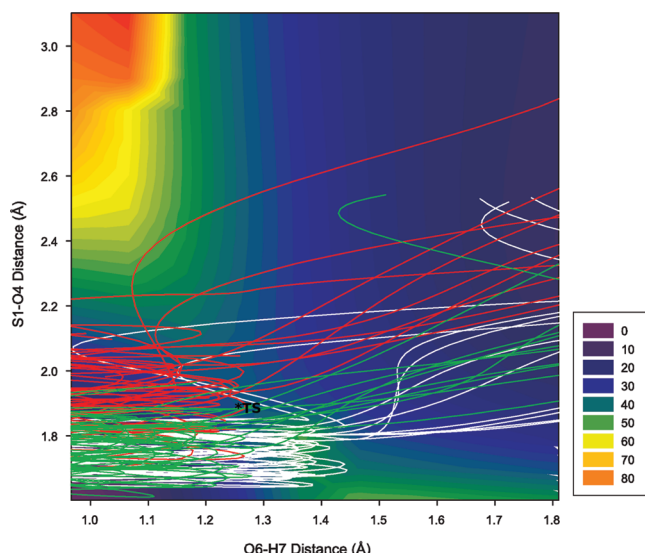


Figure 4. Calculated PES for hydrolysis of H_2SO_4 in the space defined by distances O6—H7 and S1—O4 at the MP2/6-311G++(2d,2p) level. Color lines represent different reactive trajectories for $\nu_9 = 5$: 10 trajectories with $\tau \approx 5$ ps (white), 10 trajectories with $\tau \approx 250$ ps (green), and 10 trajectories with $\tau \approx 600$ ps (red).

be included in order to correctly account for the asymptotic energetics. Thus, the ARMD simulations were run with one educt state (H_2SO_4) and two product states ($\text{SO}_3 + \text{H}_2\text{O}$ and $\text{SO}_3 + \text{OH} + \text{H}$) with correctly accounting for the asymptotic energetics.

As an illustration of a reactive trajectory, the potential energy as a function of time for a single ARMD trajectory (with excitation of $\nu_9 = 6$) is reported in Figure 5A, which shows equilibrated H_2SO_4 (black) and excited (nonequilibrium) H_2SO_4 (red) dissociating after ~ 37 ps. At this point, the potential energy changes considerably, indicating a transition from H_2SO_4 to $\text{SO}_3 + \text{H}_2\text{O}$. Figure 5B shows the distribution of the potential energy during the same simulation (histogram of the data in Figure 5A). Black corresponds to equilibrated H_2SO_4 fluctuating around 0 kcal/mol, and red corresponds to the vibrationally excited state, where a bivariate distribution shows two distinct populations. One fluctuates around 10 kcal/mol and corresponds to the product state ($\text{SO}_3 + \text{H}_2\text{O}$), whereas the second one fluctuates around 44 kcal/mol and characterizes the vibrationally excited educt state (H_2SO_4). Figure 5C shows the same quantities for a representative SCC-DFTB simulation. Again, the equilibrium distribution (black) is narrow, whereas the nonequilibrium and product state distributions are broad.

For ARMD the total energy for vibrationally excited H_2SO_4 fluctuates between 0 and 60 kcal/mol (Figure 5B) and overlaps with the product channel ($\text{SO}_3 + \text{H}_2\text{O}$) between 0 and 30 kcal/mol. Contrary to that, the overlap between the two distributions in the SCC-DFTB/MD simulations is shifted to higher energies (Figure 5C), despite the same level of excitation. For these two randomly selected trajectories, crossing the reactive seam occurs at higher energy in SCC-DFTB/MD simulations compared to the ARMD simulations. This also agrees with the energy profiles from Figure 3. On the basis of these two observations, it is expected that ARMD compared to SCC-DFTB/MD gives more rapid (because of the lower barrier) and more reliable (because of better capturing the reaction energetics compared to the MP2 calculations) time scales for average reaction times.

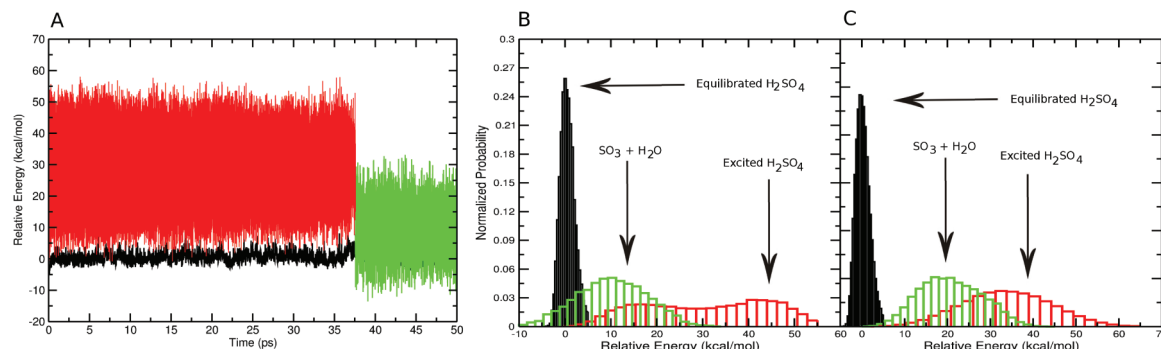


Figure 5. (A) Potential energy as a function of time for ARMD. (B) Histogram of the data in panel A. (C) Energy distribution from an SCC-DFTB simulation. Black traces correspond to equilibrated H₂SO₄, and red corresponds to H₂SO₄ excited with 61.5 kcal/mol. Bivariate distribution shows two populations corresponding to product (SO₃ + H₂O) and educt (H₂SO₄).

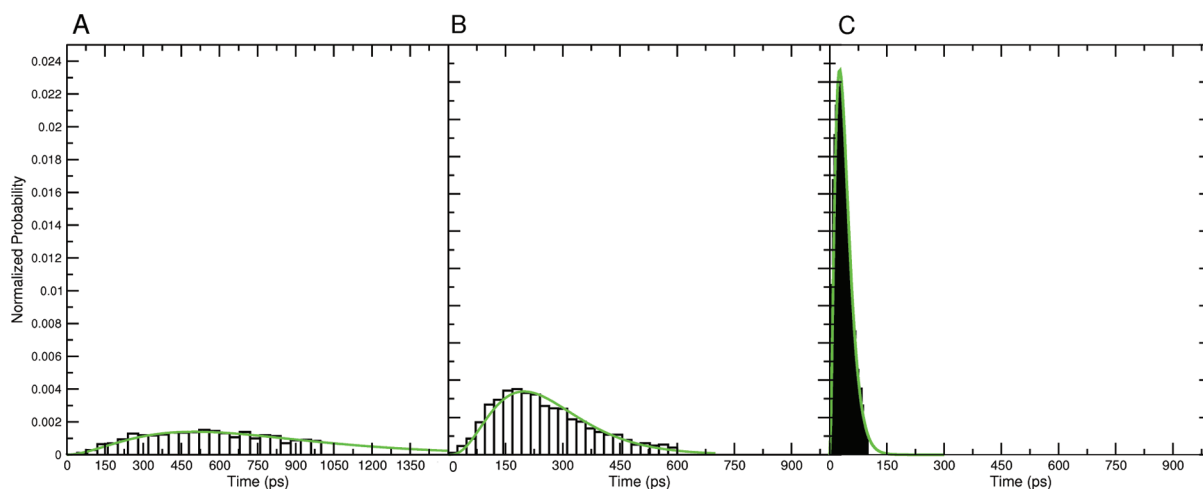


Figure 6. Normalized distribution of dissociation times $p(\tau)$ from ARMD simulations with excitation of $\nu_9 = 4$ (A), $\nu_9 = 5$ (B), and $\nu_9 = 6$ (C). The green curves represent fits of the data to a Γ -distribution (see text). Note the different t axes in the three panels. Average dissociation times are 753, 201, and 40 ps for $\nu_9 = 4$, $\nu_9 = 5$ and $\nu_9 = 6$, respectively.

Initially, 5000 ARMD simulations were run for 100 ps. For excitation of $\nu_9 = 4$, a total of 96 (2%) dissociation events ($\text{H}_2\text{SO}_4 \rightarrow \text{SO}_3 + \text{H}_2\text{O}$) out of the 5000 trajectories was observed. This fraction increased to 683 (14%) for $\nu_9 = 5$ and 3015 (60%) for $\nu_9 = 6$. Therefore, the dissociation probability is a strong function of the excitation energy, as expected. Because for $\nu_9 = 4$ and $\nu_9 = 5$ only a small fraction of trajectories lead to dissociation, the trajectories were continued to $t_{\max} = 200$ ps. This increases the number of dissociative trajectories to 6% (324 events) and 34% (1707 events) for $\nu_9 = 4$ and $\nu_9 = 5$, respectively. To further improve the quality of $p(\tau)$, which is the distribution of dissociation times, the simulation time was increased to 1 ns for $\nu_9 = 4$ and to 600 ps for $\nu_9 = 5$, which finally leads to 56% and 87% of dissociation events for $\nu_9 = 4$ and $\nu_9 = 5$, respectively.

The distributions of dissociation times $p(\tau)$ are reported in Figures 6A to C for all levels of excitation considered. The distributions $p(\tau)$ can be conveniently characterized by Γ -distributions, which represent a probabilistic model for waiting times:

$$f(x; k, \theta) = x^{k-1} e^{-x/\theta} / (\theta^k \Gamma(k)) \quad (3)$$

Here, k is a shape parameter and θ is a scale parameter, both of which are positive, and $\Gamma(k)$ is the Γ function. The mean of the

Γ distribution is $k\theta$, from which average dissociation times of $\tau_d = 201$ ps (for $\nu_9 = 5$) and $\tau_d = 40$ ps (for $\nu_9 = 6$) are obtained. Thus, by exciting the OH stretching mode with 61.5 kcal/mol, photo-dissociation is faster by almost 1 order of magnitude compared to excitation with 47.2 kcal/mol.

An alternative to ARMD are “on the fly” MD simulations with interactions calculated at an affordable (quantum or semiempirical) computational level. Such a model is SCC-DFTB, which for the present case allows one to run several hundred extended SCC-DFTB/MD simulations. The potential energy distribution for a single trajectory (with $\nu_9 = 6$) is reported in Figure 5C. However, such trajectories are computationally much more demanding than ARMD. Therefore, only 280 trajectories, each 1 ns in time, were run with 61.5 kcal/mol of excess energy. A total of 101 dissociation events (36%) was observed. This compares with a dissociation probability of 60% from 100 ps simulations based on the parametrized force field. The distribution of reaction times, $p(\tau)$, is reported in Figure S2 (Supporting Information) and demonstrates that the average reaction time is considerably longer with SCC-DFTB/MD than for ARMD simulations with the same excitation energy. This reflects the higher activation energy for SCC-DFTB (46.5 kcal/mol) compared to the force field (40.0 kcal/mol; see Figure 3). On the basis of the finding

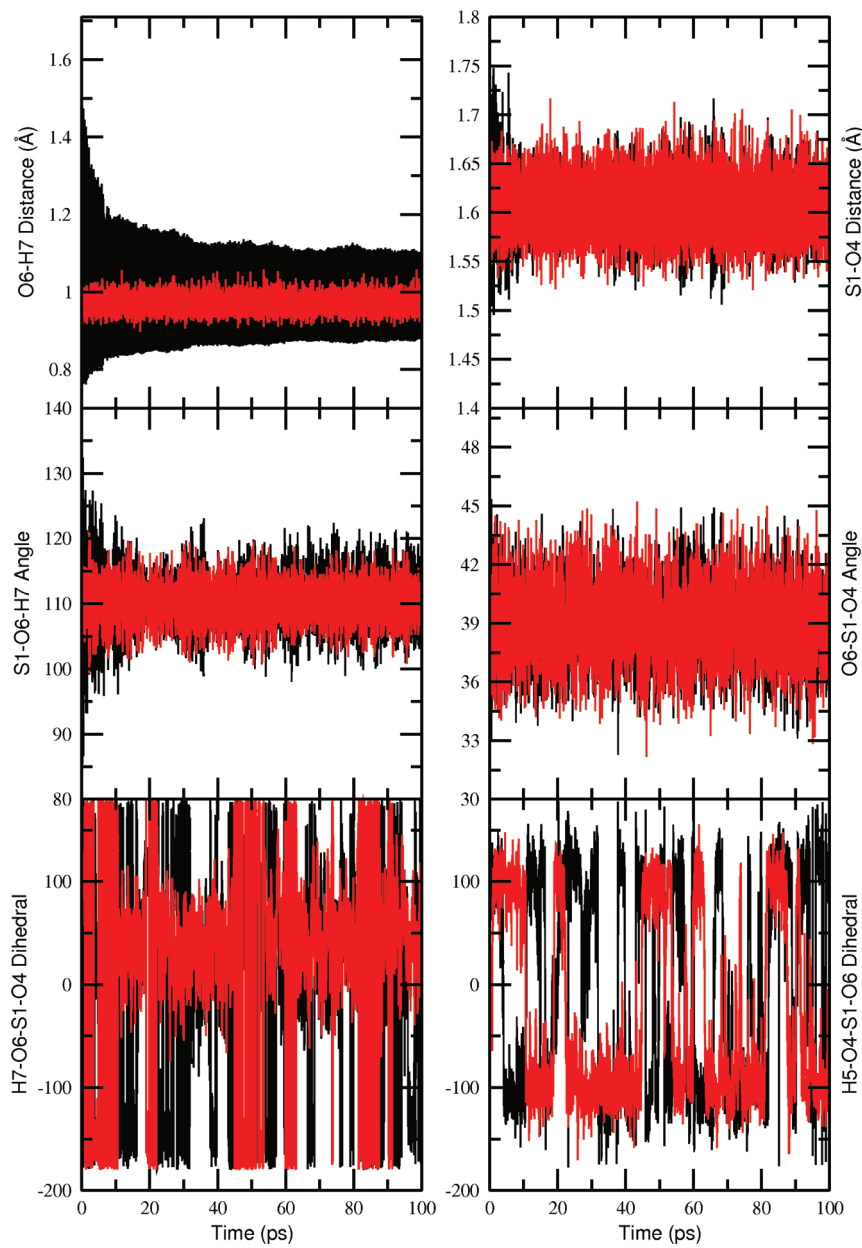


Figure 7. Time evolution of different coordinates for vibrationally excited $\nu_9 = 6$ H_2SO_4 along the normal mode involving the (O6–H7) bond in a water droplet. The equilibrated system is shown as the red trace, whereas the black trace corresponds to vibrationally excited H_2SO_4 . Note the very rapid initial decay along the vibrationally excited O6–H7 bond, which prevents the system from undergoing vibrationally assisted photodissociation.

that SCC-DFTB overestimates the energy barrier for the reaction, this result is not surprising. Furthermore, compared to MP2 and the force field parametrization, semiempirical DFTB is not sufficiently accurate to capture other important characteristics of the PES, including torsional barriers. On the other hand, SCC-DFTB also finds both physically relevant processes for the decomposition: statistical and nonstatistical vibrationally induced photodissociation.

E. Dissociation of Sulfuric Acid in a Water Droplet. In order to demonstrate the possibilities ARMD can offer to study reactive processes, and to compare with previous efforts on the binary H_2SO_4 –water complexes, we also briefly consider dissociation of sulfuric acid in a water droplet. However, it should be noted that this process is probably not relevant in the atmosphere because previous work has shown that only three water molecules are

sufficient to induce deprotonation, i.e., formation of HSO_4^- .⁴⁰ Therefore, it is expected that in solution the ionic species HSO_4^- is more prevalent than neutral H_2SO_4 . Hydrolysis of sulfuric acid has previously been investigated for hydrated H_2SO_4 .^{2,14} With one water molecule it was proposed that due to the lower barrier (25 kcal/mol) for the dissociation of $\text{H}_2\text{SO}_4 \cdot \text{H}_2\text{O}$ compared with the reaction in gas phase, the process could occur by exciting $\nu_9 \geq 3$.^{10,14} However, dynamics studies of the same system in 100 different trajectories reported no dissociation, but the decomposition of the cluster into the monomers H_2SO_4 and H_2O was observed.¹⁵ Therefore, photo-dissociation of H_2SO_4 in water is likely to be suppressed due to collisions with surrounding molecules.¹⁷

This is in fact what the present simulations find as well. None of the 100 trajectories exhibited vibrationally induced dissociation.

Contrary to excitation in the gas phase, internal energy redistribution within H_2SO_4 is unlikely, as collisions with surrounding water molecules occur. This energy flow, which takes place on a picosecond time scale, is irreversible and considerably reduces the probability for vibrationally induced photodissociation of solvated H_2SO_4 . Figure 7 reports different internal coordinates of equilibrated (red) and vibrationally excited (black) H_2SO_4 as a function of simulation time for a single trajectory. The results demonstrate that the vibrationally excited O6–H7 bond relaxes on the picosecond time scale without transferring the energy to other internal modes. Rather, the vibrational energy is lost through collisions with surrounding water molecules. Thus, the present simulations support the finding that vibrational energy flow to surrounding degrees of freedom is sufficiently rapid to suppress vibrational dissociation of H_2SO_4 .

IV. DISCUSSION

In the present work, dissociation of H_2SO_4 into $\text{SO}_3 + \text{H}_2\text{O}$ was investigated by ARMD from a statistically significant number of events following vibrational excitation of the O–H stretching vibration. It was found that starting from $\nu_9 = 4$ the reaction occurs on the picosecond to nanosecond time scale. Photodissociation on the picosecond time scale is observed upon excitation with ~ 50 kcal/mol, which corresponds to $\nu_9 \geq 5$. This supports previous conclusions based on ab initio calculations¹³ and PM3/MD simulations.¹⁵

So far, semiempirical PM3, force field-based, and SCC-DFTB methods have been used to study the energetics and dynamics of sulfuric acid dissociation following vibrational excitation. Therefore, a comparison of the three methods is quite instructive. For H_2SO_4 geometries between MP2/6-311++G(2d,2p) and the parametrized force field differ by 0.002 Å for all bonds and 2.1° for all angles. This compares with 0.024 Å and 2.7° in comparing SCC-DFTB with the MP2 calculations and deviations of up to 0.1 Å and between 1.1 and 4.6° for PM3 relative to MP2/TZP for HNO_3 and *cis*- and *trans*-HONO⁴¹ and less than 2% for bonds and 6% for angles for H_2SO_4 .¹⁷ For harmonic frequencies, reported average differences⁴¹ between MP2/TZP and PM3 for HNO_3 and *cis*- and *trans*-HONO are 130 cm⁻¹, compared to 78 cm⁻¹ for the parametrized force field and 61 cm⁻¹ for SCC-DFTB. Finally, the activation energy for H-transfer from MP2/6-311++G(2d,2p) calculations is 32.8 kcal/mol compared with 42.8 kcal/mol from PM3,¹⁷ 40.0 kcal/mol from the parametrized force field, and 46.5 from SCC-DFTB. These comparisons suggest that the parametrized force field performs best for structures and energetic barriers, whereas SCC-DFTB is on average slightly better for frequencies. The barrier for H-transfer from PM3 is somewhat higher than that from the force field. However, direct comparison for all, geometric, spectroscopic, and energetic data is somewhat difficult because for the performance of PM3 only explicit data for HNO_3 and *cis*/*trans*-HONO were available. The most relevant quantity for the present work is the barrier for H-transfer, which is best captured by the parametrized force field.

Reaction times with $\nu_9 \geq 5$ range from 6 to several hundred picoseconds, respectively. To better understand the mechanism leading to dissociation, individual trajectories were considered in more detail. This was done for very rapid, average and long reaction times for the two excitation energies. Trajectories with reaction times of $\tau = 6, 244$, and 589 ps for excitation of $\nu_9 = 5$, and $\tau = 7, 50$, and 98 ps for $\nu_9 = 6$, respectively, were analyzed. The analysis focused in particular on the time scale and degree of

energy redistribution after vibrational excitation of the OH-bond. Figure 8 reports the time series for different internal coordinates. Three types of processes can be distinguished: (i) impulsive hydrogen hopping for which no internal vibrational relaxation (IVR) is found (see Figure 8, columns A and D); (ii) partial IVR (Figure 8, columns B and E); and (iii) almost complete IVR where the vibrational energy leaks into other degrees of freedom before returning into the dissociative coordinate after many vibrational periods (Figure 8, columns C and F). For process (iii), the amplitude of the OH stretching vibration decays to levels comparable to the equilibrium simulations before dissociation occurs without, however, reaching it. In view of previously reported RRKM rates, this is relevant because direct comparison of k_{RRKM} with rates from the present work would require complete redistribution of the energy following vibrational excitation. We would, therefore, expect that even the longest reaction times from the present work are still faster than k_{RRKM} , which is what is found (see below).

For $\nu_9 = 5$ energy redistribution can occur on time scales of several hundred picoseconds before the actual reaction takes place. The initial energy is predominantly redistributed into angular and torsional degrees of freedom from where it flows back into the dissociative coordinate and the reaction takes place. This differs from simulations with 61.5 kcal/mol of available excess energy where only partial energy redistribution is observed. Under such circumstances, impulsive H-hopping is the dominant process. The same observation was made in previous simulations where partial energy redistribution was observed, and H-hopping was the proposed mechanism for dissociation in H_2SO_4 .¹⁵ For events more characteristic of the most probable reaction time ($\tau > 40$ ps), partial to almost complete IVR is observed. Considering the torsional degrees of freedom, isomerization from C_2 to C_s was observed in all trajectories. Figure 8 (bottom) shows a free energy barrier of 4.3 kcal/mol, which is in good agreement with previous studies of rotamers for H_2SO_4 .³⁵ The isomerization between C_2 and C_s is more pronounced when IVR occurs following vibrational excitation. On the contrary, when no IVR is seen and the kinetics of the reaction is faster, isomerization dynamics is virtually absent (see black curves in columns A and D, Figure 8 bottom).

Two different regimes of the reaction can therefore be distinguished: (i) Impulsive, rapid, and nonstatistical H-transfer where one of the hydroxyl-H atoms is transferred to the other OH resulting in SO_3 and H_2O formation. This model was the predominant channel found in earlier work (4 trajectories out of 98 in total based on PM3/MD simulations).¹⁵ (ii) Photodissociation following partial or complete intramolecular vibrational energy redistribution (IVR), whereby the vibrational energy is redistributed among all remaining degrees of freedom of H_2SO_4 . It should be emphasized that with the present approach the distribution of reaction times can be converged arbitrarily well because a sufficient number of trajectories can be run. Previous work required one to resort to separate computations for the two processes and did not allow one to treat them on an equal footing.^{15,17} The RRKM rates from the statistical treatment are 1.7×10^{-7} , 8.9×10^{-9} , and 1.1×10^{-9} s for $\nu_9 = 4, 5$, and 6 quanta. This compares with average reaction times of $\tau_d = 7 \times 10^{-10}$, 2×10^{-10} , and 4×10^{-11} from the present work. However, the average reaction times τ_d do not correspond to the statistical limit. Rather, complete energy redistribution requires probably at least 1 order of magnitude more time (see Figure 8), which brings the RRKM and explicitly simulated decomposition

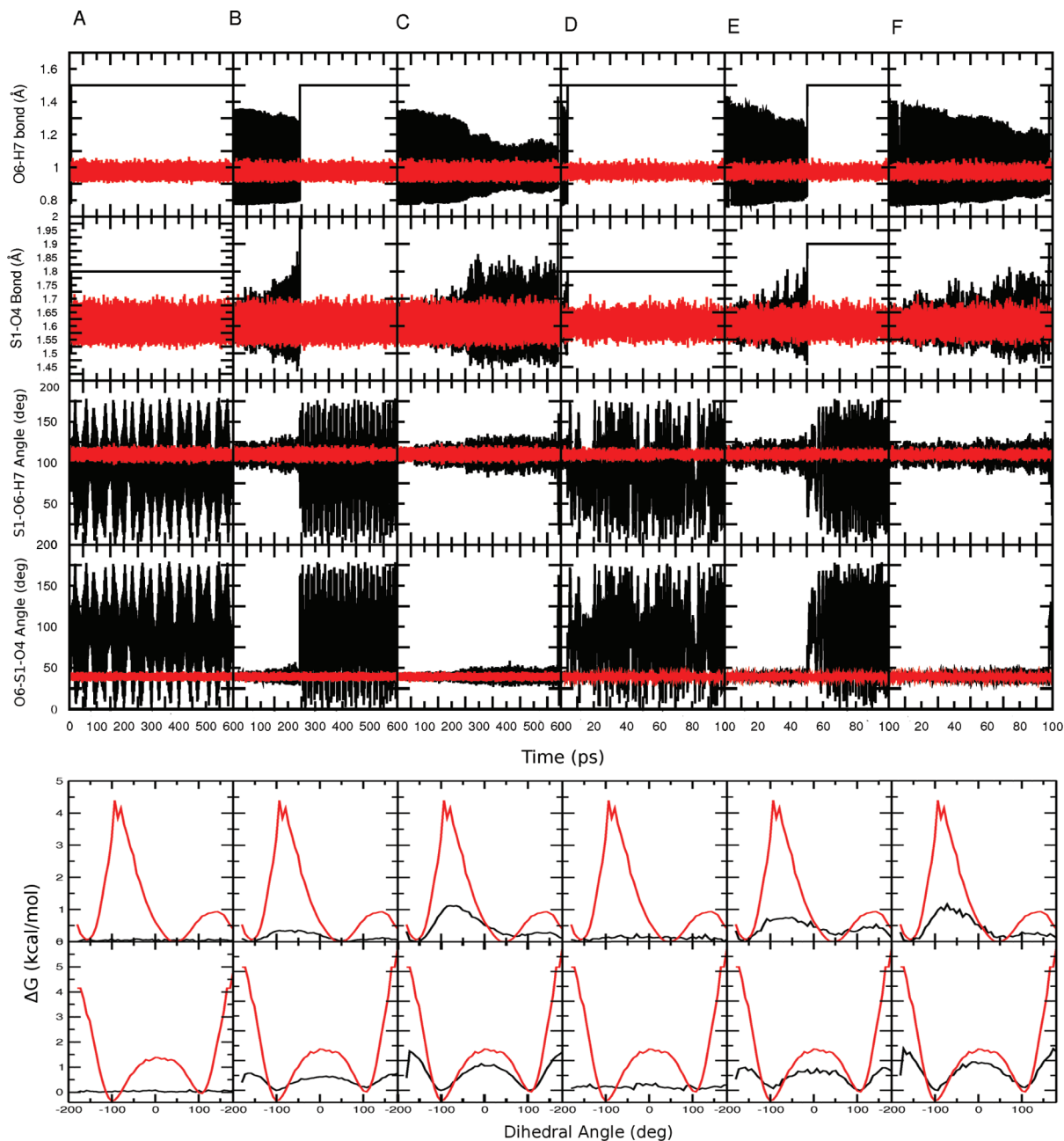


Figure 8. Coordinates of sulfuric acid in the gas phase as a function of time. Black traces correspond to the vibrationally excited state, and red corresponds to the equilibrated system (i.e., before excitation). Columns A–C are for excitation of $\nu_9 = 5$; columns D–F are for $\nu_9 = 6$. Columns show reaction time in the next order: (A) $\tau = 6$ ps, (B) $\tau = 244$ ps, (C) $\tau = 589$ ps, (D) $\tau = 7$ ps, (E) $\tau = 50$ ps, and (F) $\tau = 98$ ps. Trajectories with rapid, average, and long reaction times are shown for both cases (for details see text). From top to bottom, the amplitudes of the O6–H7 bond, S1–O4 bond, S1–O6–H7 angle, and O6–S1–O4 angle are shown. Rows 5 and 6 report Gibbs free energy as a function of the dihedral angles (H5–O4–S1–O6 and H7–O6–S1–O4).

times within about 1 order of magnitude. A possible reason for the remaining difference is in the way the different degrees of freedom couple and exchange energy with each other, which is included in the atomistic simulations but not in the RRKM theory.

In order to characterize whether structure or dynamics drives the process, the following situations were considered in more detail. 100 trajectories with excitation of $\nu_9 = 5$ were randomly selected with reaction times longer than 500 ps. In such trajectories, IVR is essentially complete. Likewise, 100 trajectories from simulations with 61.5 kcal/mol of excess energy were randomly

chosen provided that they showed dissociation within 60 ps of vibrational excitation. In such trajectories IVR is incomplete. For every trajectory, coordinates and velocities of all atoms were recorded 5 ps prior to photodissociation. Next, (i) every structure was started with all 100 velocities, and (ii) every velocity file was used with all 100 structures and the reaction time was recorded. This gives a total of 10 000 combinations, and every one of them was propagated for 200 ps for $\nu_9 = 5$ and for 100 ps for $\nu_9 = 6$. Figure 9 shows that in both cases the reaction probability is not skewed toward either structure or dynamics.

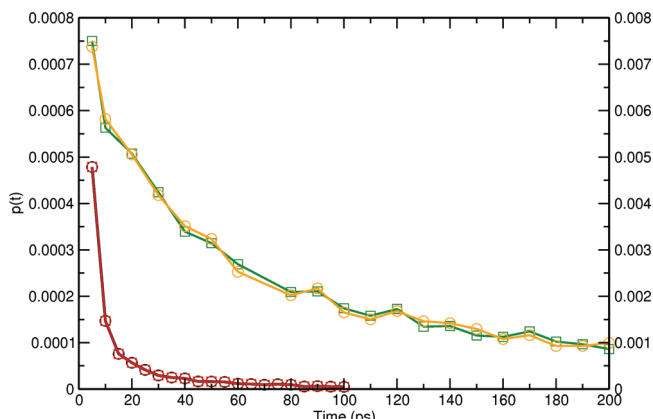


Figure 9. Dissociation probability as a function of time. The green and red curves report reaction times when individual coordinates are combined with all velocities. The orange and black curves correspond to combining individual velocities with all coordinates. Red and black curves refer to $v_9 = 6$, in the same way orange and green curves refer to $v_9 = 5$. For details see text.

The decay times for $v_9 = 6$ are about an order of magnitude more rapid compared to those for $v_9 = 5$ (see Figure 9). This again suggests that for $v_9 = 5$ dissociation is predominantly driven by IVR, whereas for $v_9 = 6$ H-hopping is the more likely process. However, no preference of a “dynamically” over a “structurally” driven process could be found.

V. CONCLUSION

In conclusion, extensive ARMD simulations with tailored force fields support the hypothesis that in the gas phase (and at higher altitudes in the atmosphere), vibrational excitation of $v_9 > 4$ leads to photodissociation of H_2SO_4 into $\text{SO}_3 + \text{H}_2\text{O}$. Typical average reaction times for $v_9 \geq 4$ are on the picosecond time scale or faster. Given that the parametrized force field overestimates the reaction barrier by ~ 7 kcal/mol, all reaction times reported here are probably 2 orders of magnitude too slow. However, this does not affect the general conclusion that dissociation through vibrational excitation of $v_9 = 4$ or higher OH-overtone in H_2SO_4 is a process that occurs on the picosecond time scale. Mechanistically, anything between impulsive H-transfer (sub-picoseconds) to almost complete IVR with subsequent dissociation (picoseconds to nanoseconds) are observed. The time scales found from the present simulations agree qualitatively with those from separate previous investigations and are, to our knowledge, the first that cover the entire range of dynamics following overtone excitation of H_2SO_4 . Such types of simulations hold much promise to provide atomistically detailed pictures of reactive processes, not only for large biomolecular systems but also for activated processes in the gas phase and in clusters.²²

■ ASSOCIATED CONTENT

S Supporting Information. Details on the force field parameters and distribution times from the SCC-DFTB/MD simulations. This material is available free of charge via the Internet at <http://pubs.acs.org>.

■ ACKNOWLEDGMENT

The authors gratefully acknowledge financial support from the Swiss National Science Foundation through Grants 200021-117810

(to M.M.) and 200021-124936 (NCCR Molecular Ultrafast Science and Technology (MUST)). We thank Dr. S. Lutz for stimulating discussions.

■ REFERENCES

- Clement, F.; Ford, I. *J. Atmos. Environ. A: Gen* **1999**, *33*, 475–487.
- Larson, L. J.; Kuno, M.; Tao, F. M. *J. Chem. Phys.* **2000**, *112*, 8830–8838.
- Hofmann, D. J.; Rosen, J. M. *Nature* **1982**, *297*, 120–124.
- Raes, F.; Dingenen, R. V.; Vignati, E.; Wilson, J.; Pataud, J.-P.; Seinfeld, J. H.; Adams, P. *Atmos. Environ. A: Gen* **2000**, *34*, 4215–4240.
- Duplissy, J.; et al. *Atmos. Environ. A: Gen* **2010**, *10*, 1635–1647.
- Rinsland, C.; Gunson, M.; Ko, M.; Weisenstein, D.; Zander, R.; Abrams, M.; Goldman, A.; Sze, N.; Yue, G. *Geophys. Res. Lett.* **1995**, *22*, 1109–1112.
- Hintze, P. E.; Kjaergaard, H. G.; Vaida, V.; Burkholder, J. B. *J. Chem. Phys.* **2003**, *107*, 1112–1118.
- Vaida, V. *J. Phys. Chem. A* **2009**, *113*, 5–18.
- Seinfeld, J.; Pandis, S. *Atmospheric Chemistry and Physics From Air Pollution to Climate Change*; John Wiley and Sons: New York, 1998.
- Vaida, V.; Kjaergaard, H. G.; Hintze, P. E.; Donaldson, D. J. *Science* **2003**, *299*, 1566–1568.
- Donaldson, D.; Frost, G.; Rosenlof, K.; Tuck, A. F.; Vaida, V. *Geophys. Res. Lett.* **1997**, *24*, 2651–2654.
- Donaldson, D. J.; Tuck, A. F.; Vaida, V. *Chem. Rev.* **2003**, *103*, 4717–4729.
- Feierabend, K. J.; Havey, D. K.; Brown, S. S.; Vaida, V. *Chem. Phys. Lett.* **2006**, *420*, 438–442.
- Morokuma, K.; Muguruma, C. *J. Am. Chem. Soc.* **1994**, *116*, 10316–10317.
- Miller, Y.; Gerber, R. B. *J. Am. Chem. Soc.* **2006**, *128*, 9594–9595.
- Gerber, R. B. University of California, Irvine, School of Physical Sciences; Private communication, 2011.
- Miller, Y.; Gerber, R. B.; Vaida, V. *Geophys. Res. Lett.* **2007**, *34*, 1–5.
- Carpenter, B. K. *Annu. Rev. Phys. Chem.* **2005**, *56*, 57–89.
- Danielsson, J.; Meuwly, M. *J. Chem. Theory. Comput.* **2008**, *4*, 1083–1093.
- Nutt, D.; Meuwly, M. *Biophys. J.* **2006**, *90*, 1191–1201.
- Mishra, S.; Meuwly, M. *Biophys. J.* **2006**, *96*, 2105–2118.
- Lutz, S.; Meuwly, M. *ChemPhysChem* **2011**, DOI: 10.1002/cphc.201100575.
- Brooks, B. R.; Bruccoleri, R. E.; Olafson, B. D.; States, D. J.; Swaminathan, S.; Karplus, M. *J. Comput. Chem.* **1983**, *4*, 187–217.
- Nguyen, P. N.; Stock, G. *J. Chem. Phys.* **2003**, *119*, 11350–11358.
- Meuwly, M.; Müller, A.; Leutwyler, S. *Phys. Chem. Chem. Phys.* **2003**, *5*, 2663–2672.
- Jorgensen, W.; Chandrasekhar, J.; Madura, J.; Impey, R.; Klein, M. *J. Chem. Phys.* **1983**, *79*, 926–935.
- Frisch, M. J. et al. *Gaussian 03*, revision C.01; Gaussian, Inc.: Wallingford CT, 2004.
- Law, M.; Hutson, J. *Comput. Phys. Commun.* **1997**, *102*, 252–268.
- Devereux, M.; Meuwly, M. *J. Chem. Inf. Model.* **2010**, *50*, 349–357.
- Halgren, T.; Lipscomb, W. *Chem. Phys. Lett.* **1977**, *49*, 225–232.
- Gonzales, C.; Schlegel, H. *J. Chem. Phys.* **1989**, *90*, 2154–2161.
- Elstner, M.; Porezag, D.; Jungnickel, G.; Elsner, J.; Haugk, M.; Frauenheim, T.; Suhai, S.; Seifert, G. *Phys. Rev. B* **1998**, *58*, 7260–7268.
- Demaison, J.; Herman, M.; Lievin, J.; Rudolph, H. D. *J. Phys. Chem. A* **2007**, *111*, 2602–2609.
- Lohr, L. *J. Mol. Struct. (THEOCHEM)* **1982**, *4*, 221–227.
- Havey, D. K.; Feierabend, K. J.; Vaida, V. *J. Mol. Struct. (THEOCHEM)* **2004**, *680*, 243–247.
- Sabin, J.; Brandas, E.; Goodsite, M. E.; Johnson, M. *Advances in Quantum Chemistry. Applications of Theoretical Methods to Atmospheric Science*; Elsevier: New York, 2008.
- Sedo, G.; Schltz, J.; Leopold, R. *J. Mol. Spectrosc.* **2008**, *251*, 4–8.

- (38) Ruscic, B.; Feller, D.; Dixon, D.; Peterson, K.; Harding, L.; Asher, R. A. *W. J. Phys. Chem. A* **2001**, *105*, 1–4.
- (39) Fanourgakis, S.; Xantheas, S. *J. Chem. Phys.* **2008**, *128*, 07450601–07460611.
- (40) Arstila, H.; Laasonen, K.; Laaksonen, A. *J. Chem. Phys.* **1998**, *108*, 1031–1039.
- (41) Miller, Y.; Chaban, G.; Finlayson-Pitts, B.; Gerber, R. *J. Phys. Chem. A* **2006**, *110*, 5342–5354.